

Elemental composition x-ray fluorescence analysis with a TES-basedhigh-resolution x-ray spectrometer

Bingjun Wu(吴秉骏), Jingkai Xia(夏经铠), Shuo Zhang(张硕), Qiang Fu(傅强), Hui Zhang(章辉), Xiaoming Xie(谢晓明), and Zhi Liu(刘志)

Citation: Chin. Phys. B, 2023, 32 (**9**): 097801. DOI: 10.1088/1674-1056/acd926
Journal homepage: http://cpb.iphy.ac.cn; http://iopscience.iop.org/cpb

What follows is a list of articles you may be interested in

Transition-edge sensors using Mo/Au/Au tri-layer films

Hubing Wang(王沪兵), Yue Lv(吕越), Dongxue Li(李冬雪), Yue Zhao(赵越), Bo Gao(高波), and Zhen Wang(王镇)
Chin. Phys. B, 2023, 32 (**2**): 028501. DOI: 10.1088/1674-1056/ac7f94

Multiplexing technology based on SQUID for readout of superconducting transition-edge sensor arrays

Xinyu Wu(吴歆宇), Qing Yu(余晴), Yongcheng He(何永成), Jianshe Liu(刘建设), and Wei Chen(陈炜)
Chin. Phys. B, 2022, 31 (**10**): 108501. DOI: 10.1088/1674-1056/ac693c

Effect of different catalysts and growth temperature on the photoluminescence properties of zinc silicate nanostructures grown via vapor-liquid-solid method

Ghfoor Muhammad, Imran Murtaza, Rehan Abid, and Naeem Ahmad
Chin. Phys. B, 2022, 31 (**5**): 057801. DOI: 10.1088/1674-1056/ac439e

Development of series SQUID array with on-chip filter for TES detector

Wentao Wu(伍文涛), Zhirong Lin(林志荣), Zhi Ni(倪志), Peizhan Li(李佩展), Tiantian Liang(梁恬恬), Guofeng Zhang(张国峰), Yongliang Wang(王永良), Liliang Ying(应利良), Wei Peng(彭炜), Wen Zhang(张文), Shengcai Shi(史生才), Lixing You(尤立星), and Zhen Wang(王镇)
Chin. Phys. B, 2022, 31 (**2**): 028504. DOI: 10.1088/1674-1056/ac2b91

Temperature and current sensitivity extraction of optical superconducting transition-edge sensors based on a two-fluid model

Yue Geng(耿悦), Pei-Zhan Li(李佩展), Jia-Qiang Zhong(钟家强), Wen Zhang(张文), Zheng Wang(王争), Wei Miao(缪巍), Yuan Ren(任远), and Sheng-Cai Shi(史生才)
Chin. Phys. B, 2021, 30 (**9**): 098501. DOI: 10.1088/1674-1056/ac11ce

---

INSTRUMENTATION AND MEASUREMENT

Elemental composition x-ray fluorescence analysis with a TES-based high-resolution x-ray spectrometer

Bingjun Wu(吴秉骏)[1,2,5,†], Jingkai Xia(夏经铠)[2,†], Shuo Zhang(张硕)[2,‡], Qiang Fu(傅强)[2,3], Hui Zhang(章辉)[1], Xiaoming Xie(谢晓明)[1,4,5], and Zhi Liu(刘志)[1,2,3,§]

[1] *State Key Laboratory of Functional Materials for Informatics, Shanghai Institute of Microsystem and Information Technology, Chinese Academy of Sciences, Shanghai* 200050, *China*

[2] *Center for Transformative Science, ShanghaiTech University, Shanghai* 201210, *China*

[3] *School of Physical Science and Technology, ShanghaiTech University, Shanghai* 201210, *China*

[4] *Center for Excellence in Superconducting Electronics, Chinese Academy of Sciences, Shanghai* 200050, *China*

[5] *University of Chinese Academy of Sciences, Beijing* 100049, *China*

(Received 18 April 2023; revised manuscript received 25 May 2023; accepted manuscript online 26 May 2023)

The accurate analysis of the elemental composition plays a crucial role in the research of functional materials. The emitting characteristic x-ray fluorescence (XRF) photons can be used for precisely discriminating the specified element. The detection accuracy of conventional XRF methodology using semiconductor detector is limited by the energy resolution, thus posing a challenge in accurately scaling the actual energy of each XRF photon. We adopt a novel high-resolution x-ray spectrometer based on the superconducting transition-edge sensor (TES) for the XRF spectroscopy measurement of different elements. Properties including high energy resolution, high detection efficiency and precise linearity of the new spectrometer will bring significant benefits in analyzing elemental composition via XRF. In this paper, we study the *L*-edge emission line profiles of three adjacent rare earth elements with the evenly mixed sample of their oxide components: terbium, dysprosium and holmium. Two orders of magnitude better energy resolution are obtained compared to a commercial silicon drift detector. With this TES-based spectrometer, the spectral lines overlapped or interfered by background can be clearly distinguished, thus making the chemical component analysis more accurate and quantitative. A database of coefficient values for the line strength of the spectrum can then be constructed thereafter. Equipped with the novel XRF spectrometer and an established coefficient database, a direct analysis of the composition proportion of a certain element in an unknown sample can be achieved with high accuracy.

Keywords: x-ray emission spectra and fluorescence, superconducting transition-edge sensor, rare earth elements, chemical composition analysis

PACS: 78.70.En, 85.25.Oj, 71.20.Eh, 81.70.Jb **DOI:** 10.1088/1674-1056/acd926

1. Introduction

The accurate analysis of the composition of each element in a compound is an essential and indispensable aspect of material analysis research. The chemical properties of different compounds, in the particular case of rare earth oxides (REOs), are determined by the specific composition and bonding behavior of different rare earth elements (REEs), highlighting the importance of precise determination of elemental composition in these materials.[1,2] And further in the practical research and application of the rare earth functional material, the trace level doped REEs with slightly different chemical compositions will lead to changes in the properties, which can be mainly attributed to the particularity of the electronic configuration of REEs.[1,3] In order to accurately determine the chemical composition of trace REEs in materials under laboratory conditions, it is necessary to adopt advanced analytical techniques like the methodology of x-ray fluorescence (XRF), which is crucial for gaining insight into more potential applications of REOs.[4–6] In XRF, the electron within the sample atom is excited when irradiated by a primary x-ray beam. This produces a hole in the initial electron orbital and results in an unstable atomic state. Then an electron from a higher energy orbital fills the hole and emits characteristic x-ray photons with quantized energy.[5] By collecting the emitted x-ray photons and analyzing the whole fluorescence spectrum, XRF can supply a large amount of information, including the peak energies, line shapes, electron binding energies, energy level widths, fluorescence yields, etc.[7,8]

In the XRF analysis, as the x-ray line energies are distributed in a certain range with a broadened extent between shells of different *Z*-value elements, there would possibly be numerous peak overlaps, i.e., weaker spectral lines would be hidden beneath the extension range of spectral lines with higher intensity.[9–11] Such overlapping spectral feature is

[†]These authors contributed equally to this work.

[‡]Corresponding author. E-mail: shuozhang@shanghaitech.edu.cn

[§]Corresponding author. E-mail: liuzhi@shanghaitech.edu.cn

© 2023 Chinese Physical Society and IOP Publishing Ltd

usually presented in the form of an intrinsic spectral peak broadening overlap or the existence of background spectral shape.[6,12] A better understanding of peak energies and spectral profiles would aid elemental composition extraction through peak-fitting analysis. In particular, for XRF research and analyses involving REEs, L-edge emission lines of high-Z REEs are preferred over the more intense K-edge emission lines, which necessitate excitation energies beyond the capabilities of most laboratory-based x-ray sources, despite constraints caused by adjacent emission line overlap.[3,13] In addition, due to the limitation of the spectrometer resolution, the measured emission spectra of REEs may also overlap with the K-edge emission lines of 3d transition metals, such as Fe, Co, Ni, etc., which are usually with much higher abundance in natural materials.[14] The energy resolution required for those measurements has exceeded the capabilities provided by traditional elemental analysis instruments or spectroscopies, with the energy dispersive spectrometer (EDS) as one of the representatives.[11,15] Thus, in order to unravel the complicated XRF spectra with overlapping lines and to accurately measure the line energies and profiles for REEs, it is essential not only to fit and analyze the spectral data but also to explore, at a more fundamental level, the development of instruments with higher energy resolution.[16]

We present a newly developed instrument for XRF spectroscopy measurement here, which meets the experimental requirements including high detection efficiency, precise linearity and broad-band response.[16] Our scientific instrument is capable of measuring the absolute energies and line profiles of XRF emission lines, with a calibration process to linearize the energy response of each photon captured and to establish an XRF database of all other, unknown spectral features.[17–20] Our spectrometer used for this work consists of an array of 16-pixel (4×4) superconducting device called transition-edge sensor (TES), and a readout based on superconducting quantum interference device (SQUID) amplifiers.[20–22] Our detector can directly measure the energy of each incident x-ray photon, resulting in much better spectral resolution compared to a commercial silicon drift detector. The advantages of TES detectors over wavelength-dispersive grating spectrometers include a large collection area, high quantum efficiency and wide energy range, making them well-suited for studying a variety of materials and phenomena.[23,24] These attributes also enable obtaining high-resolution spectra from dilute and damage-sensitive samples, with dilutions as low as 0.001% (10 ppm), and a high P/B ratio for distinguishing weak signals from background fluctuations, which is essential for the analysis of trace elements.[20,25] Especially in the field of rare earth sciences, TES detectors have been proposed for a variety of applications, including high energy-resolution x-ray spectroscopy, material diagnostics, and mass spectrometry for neutral molecules.[11]

We have studied the L-edge emission lines of three adjacent and widely-studied REEs: terbium (Tb, $Z = 65$), dysprosium (Dy, $Z = 66$) and holmium (Ho, $Z = 67$) for digging out their intrinsic information, with the energy calibration work carried out by the K-edge emission lines of the 3d transition metal elements. All the L-edge emission lines of the selected elements, from their lowest energy levels $L_3M_1(L\lambda)$ up to the highest $L_2N_4(L\gamma_1)$, lie in a range from 5.5 keV to 9.5 keV (see Fig. 1), which also happens to be within the well-calibrated range of our instrument.[26,27] Thus, the precise L-edge emission line energies and their full line profiles of each element can be well measured and estimated.

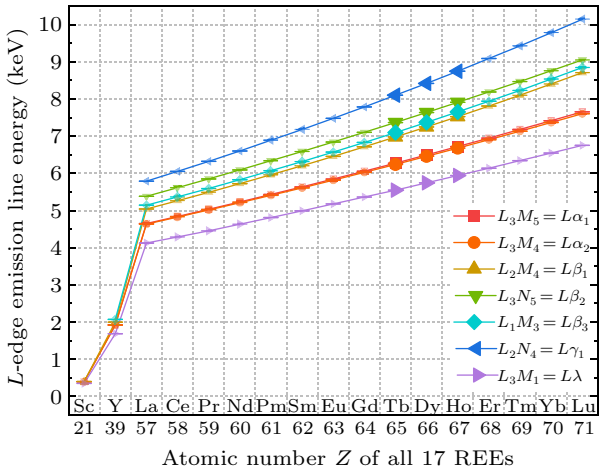


Fig. 1. Most of the L-edge emission lines of all 17 REEs are shown, with the certain selected three REEs emphasized. The energies of terbium (Tb, $Z = 65$), dysprosium (Dy, $Z = 66$) and holmium (Ho, $Z = 67$) lie in a range from 5.5 keV to 9.0 keV, with the lowest energy levels $L_3M_1(L\lambda)$ up to the highest $L_2N_4(L\gamma_1)$. Data are rebuilt from NIST database.[26,27]

2. Experimental

2.1. TES-based x-ray spectrometer

As the core component of the spectrometer, TES plays a key role in converting the energy signal into an electrical signal that can be calibrated and analyzed for statistical processing to obtain the spectrum.[28,29] The whole array of TESs is fabricated on a single silicon wafer. All TESs are operated at a superconducting transition temperature of about 90 mK, where the devices can absorb the energy of x-ray photons and be heated up to a non-superconducting state of higher temperature, and then transfer the energy to the surrounding bath by a weak thermal connection, thereby cooling back to the initial normal state.[16,30,31]

Thus, each TES consists of two components in close thermal contact: a heat absorber and a thermometer.[32] The absorbing layer of bismuth (Bi) with a thickness of about 2.4 μm and an area of about 500 μm × 500 μm can convert x-ray photons into thermal energy with an absorption efficiency of 70% at 5.9 keV. The total detection efficiency contributed by each process of x-ray photons with energies from 0 keV–10 keV

is shown in Fig. 2.[7,20,33] The molybdenum-copper double-layer film serves as a sensitive resistive thermometer, which can be held in its narrow superconducting transition by Joule self-heating. The composition and size are selected to achieve the required transition temperature and electrical resistance. Examples of the TES signal pulse diagram at various energies are shown in Fig. 3, where the amplitude of the pulses indicates the amount of energy deposited.[30]

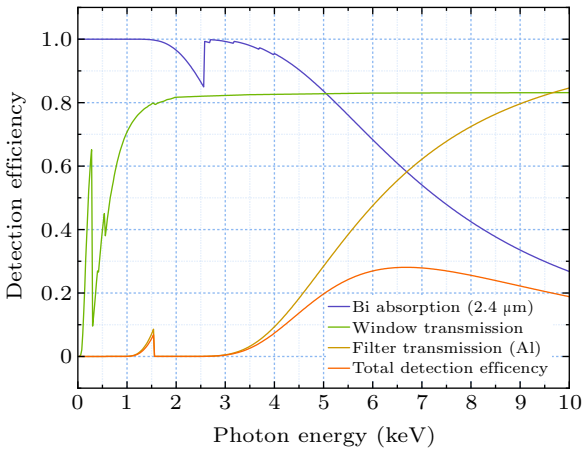


Fig. 2. The total detection efficiency can be calculated by the product of all efficiency contributed to the whole process. Within the energy range of 5 keV–10 keV, the transmission process behaves stronger as the energy increases, while the absorption process of x-ray photons becomes weaker, accomplished by the heat absorber of TESs, which are made of bismuth (Bi) with a thickness of 2.4 μm. The total detection efficiency curve can be used for further calculation of the chemical composition of measured samples. Data are generated with the online tools.[7,33]

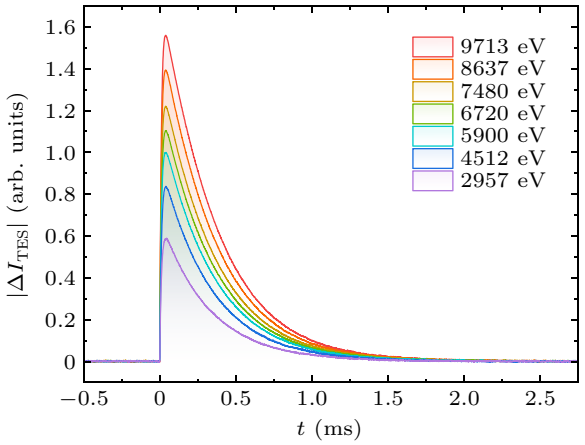


Fig. 3. The shapes of seven different current pulses of a single TES behave similarly, and the pulse amplitude indicates the amount of energy deposited. By convention, each pulse signal with a current decrease is reversely plotted as a positive relative change of TES current. The absorption of different x-ray photon energies which fully span the calibrated energy range, causes a sharp rise of temperature and resistance, accompanied by a sudden drop in the bias current, followed by a recovering procedure to the initial superconducting state within a few milliseconds.

By the connection of the molybdenum leads, these signals of the TES chips are then transmitted to the cryogenic signal amplifier, which mainly includes SQUID array operating at 4 K, room temperature feedback amplifier circuit, control circuit and cryogenic cables. The room temperature feedback amplifier circuit possesses a bandwidth of 1 MHz. The TES array and the SQUID array are both located inside an adiabatic demagnetization refrigerator (ADR). The vacuum window and a series of thin aluminum filters are adopted for blocking infrared and visible radiation.[34] A schematic diagram of the spectrometer system is shown in Fig. 4 below. The signal acquisition and analysis system mainly include analog-to-digital conversion (ADC) board, waveform analysis module and energy spectrum analysis software.[17] After the signal is transmitted to the analysis module, the pulse height is calibrated and fitted by offline analysis software, then the x-ray energy spectrum is finally obtained. After preliminary tests, the detector has an energy resolution of 5.2 eV@5.9 keV.

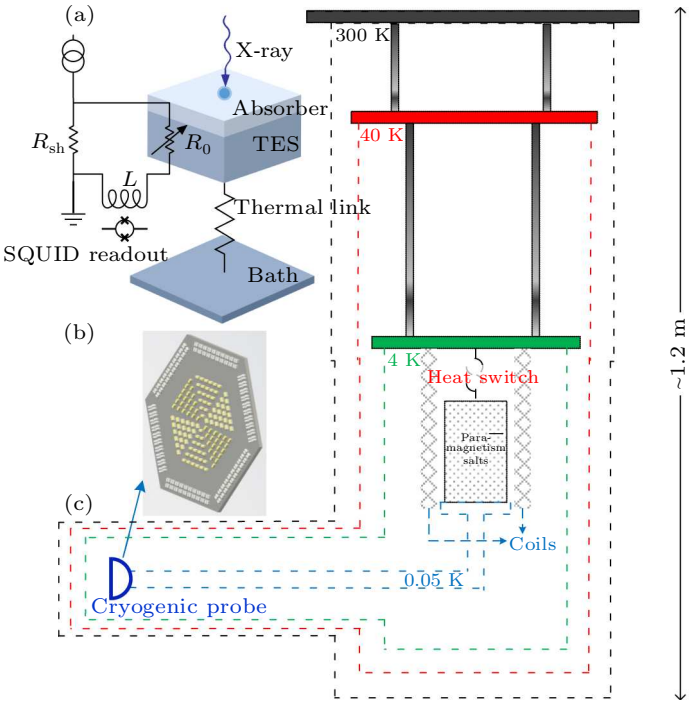


Fig. 4. (a) The schematic diagram of the TES x-ray detector. (b) TES sensors are located in the 0.05 K stage of the ADR, at the forefront of the cryogenic probe and parallel to the window. (c) The entire spectrometer system is integrated within an ADR that contains vacuum stages at various temperatures.

2.2. Samples preparation and spectrum acquisition

The tested samples are compressed from different REO powders provided by Macklin® Reagent Company, with a purity of 99.99% according to the supplier's certificate of analysis. These powdered oxides include terbium (III,IV) oxide (Tb_4O_7), dysprosium (III) oxide (Dy_2O_3) and holmium (III) oxide (Ho_2O_3). A precision electronic balance is used to weigh 100 mg of each oxide sample, and a set of tableting die and tableting machine are used to perform tableting samples on them under the same conditions. After preparation, the final compressed samples are all uniform discs with a diameter of 8 mm and a thickness of about 1 mm. Moreover, an evenly mixed sample piece of the three oxide components, fully grinded afterward and compressed under the same experimental conditions, is used for assessing the feasibility of our

testing methods. Through accurate calculation of the molecular weight of each oxide, it is ensured that the concentration of each component remains consistent and comparable.

After accomplishing the compressing operation of REO samples, these compressed samples need to be fixed on a specific sample holder in order to control the stability of experimental parameters such as x-ray irradiation position, intensity and reflection traveling path, etc., meanwhile as well ensure the repeatability of the experiment.[12] Therefore, we adopt model designing and machining to manufacture a modular-assemblable, sample-replaceable and reusable sample holder using polymethyl methacrylate (PMMA), a type of plastic material with high transparency and strong formability, as shown below in Fig. 5. The sample holder can not only meet the requirements of rapid and convenient replacement of the sliced samples, but also realize both reflection and transmission measurement modes. As the compressed samples are steadily placed into the pre-designed groove with a diameter of 8 mm and a depth of about 1 mm inside the sample holder, and the incident angle of x-ray onto the sample is precisely fixed at 45° for maximized collection, the x-ray emitted by various elements of the sample will accurately reach our TES sensors through the designed path.

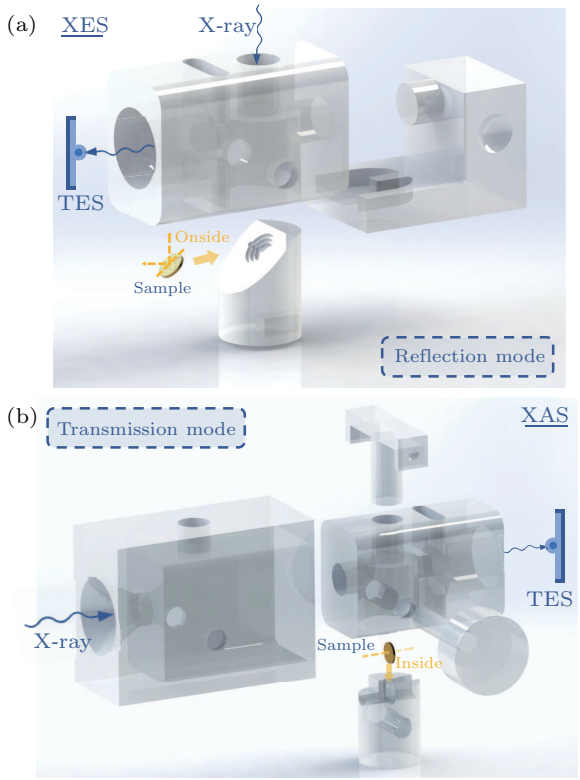


Fig. 5. Both reflection (left, XES) and transmission (right, XAS) measurement modes can be realized by adopting the modular-assemblable, sample-replaceable and reusable sample holder made of PMMA. The sliced samples ought to be placed onto or into the pre-designed groove, so as to ensure the reflected or transmitted x-ray microbeam would accurately reach the TES sensors and finally can be collected and analyzed.

A commercial miniature x-ray tube, Mini-X2 with Au anode from AMPTEK®, is adopted to generate the initial incident x-ray. The electrons are accelerated from a cathode tube with the voltage of up to 15.0 kV towards the Au anode target, ensuring obtaining both bremsstrahlung and characteristic fluorescence emission lines. The current of the tube is set to 20.0 μA, i.e., the power condition is controlled at 300 mW to stabilize the x-ray photon flux. The bias current of TES is set to 0.95 mA. The total test time per sample is about 16 h for the sufficient valid counts up to about 10^6. As is briefly explained in the introduction part previously, the incident x-ray hits the surface of the sample, thus stimulating the emitted x-ray with the *L*-edge emission lines of our elements of interest included, strikes the TES array, after traveling a distance of about 5 cm. Therefore, we ensure that only photons reflected, scattered, or absorbed and re-emitted by the target reach the sensors. When such XRF photons irradiate directly on the TESs, the energy contained in each photon is converted into a current pulse signal, and then recorded and saved. Through the accumulation of fluorescence signal data for several hours, all the pulse signals are counted according to the frequency distribution of pulse height, and the *L*-edge fluorescence spectrum of the sample in a wide energy range can be obtained. Afterwards, the pulse heights are accurately converted into energy scale by energy calibration. Then after peak fitting, the center energies, the peak shapes and the area ratio of different peaks can be accurately measured.[24,35,36]

3. Results and discussion

3.1. Calibration of the spectrometer by transition metals

As the electrical signals collected by the spectrometer needed to be accurately converted into energy-scale counts, it is a crucial step for the energy calibration process of the instrument. For calibration, we adopt samples of various 3d transition metals ($Z = 22 - 30$) as our standard samples,

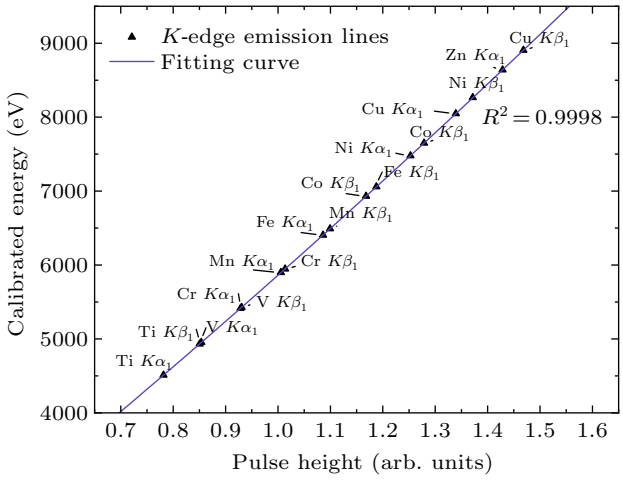


Fig. 6. The calibration curve for the XRF spectrum of one of the TES channels. Triangle anchors are obtained from the fitting results of *K*-edge emission lines of various 3d transition metals of standard samples, from Ti $K\alpha_1$ (4511 eV) to Cu $K\beta_1$ (8905 eV). The curve is well fitted according to the quadratic function, then can be utilized for the calibration process of the REOs spectrum afterward.

including titanium ($_{22}$Ti), vanadium ($_{23}$V), chromium ($_{24}$Cr), manganese ($_{25}$Mn), iron ($_{26}$Fe), cobalt ($_{27}$Co), nickel ($_{28}$Ni), copper ($_{29}$Cu), and zinc ($_{30}$Zn). Each of the *K*-edge emission lines of these 3d transition metals contributes a vital point to the total calibration curve, which happens to meet up with the working energy range of our spectrometer, as shown in Fig. 6 below. A quadratic function is selected as the fitting function to reduce the mean square error (MSE) of the calibration curve.

3.2. Energy spectrums of REEs

By the calibration process mentioned above, the XRF electrical signals of *L*-edge emission lines of all the samples are converted into the absolute energy scale, and thus the spectrum can be obtained. To compare with the energy resolution of SDD detector, the experiment of the mixed sample is taken under similar conditions for TES and SDD, as the results are shown in Fig. 7 below. The line shapes of fluorescence spectrum are usually theoretically described as the sum of multiple Lorentz (also known as Cauchy) distributions. Meanwhile, the intrinsic broadening effect of the instrument for each energy peak can be approximated to a Gaussian distribution. Therefore, the final energy spectrum is the convolution of Lorentz distribution and Gaussian distribution, which is also widely accepted as Voigt function.[37] And according to this, the peak fitting process of each calibrated energy spectrum is carried out respectively, and the relevant codes are developed and processed offline, which can achieve a large number of spectrum data batch processing. The peak fitting results of each region of the spectrum are shown in Fig. 8 below, as fitted lines of different regions are presented in Figs. 8(a)–8(d), respectively.

3.3. Composition analysis of REEs

Since the respective weights of the three REOs of the evenly mixed sample are well calculated according to the ratio of moles of REEs at 1:1:1, their theoretical contribution to the mixing energy spectrum is consistent in probability. And at the same time, due to the difference in cross section and other factors of different element atoms, there may be some slight differences in x-ray absorption and reflection coefficients. Therefore, there will be some differences in the intensity of the multiple *L*-edge peaks across elements in the energy spectrum of the mixed sample. Further, the total detection efficiency in Fig. 2 is also taken into consideration. Then, based on the intensity of each peak, we can establish a coefficient database of intensity contribution of each specific element, as shown in Fig. 9 for instance. In addition, as for analyzing the energy spectrum of samples with unknown composition for specific elements, the actual concentration of each element can be obtained by intensity of the fitted peaks of the calibrated energy spectrum. Compared with the accuracy of the element composition analysis methodology based on SDD, our methodology would contribute an advance by one or two orders of magnitude.

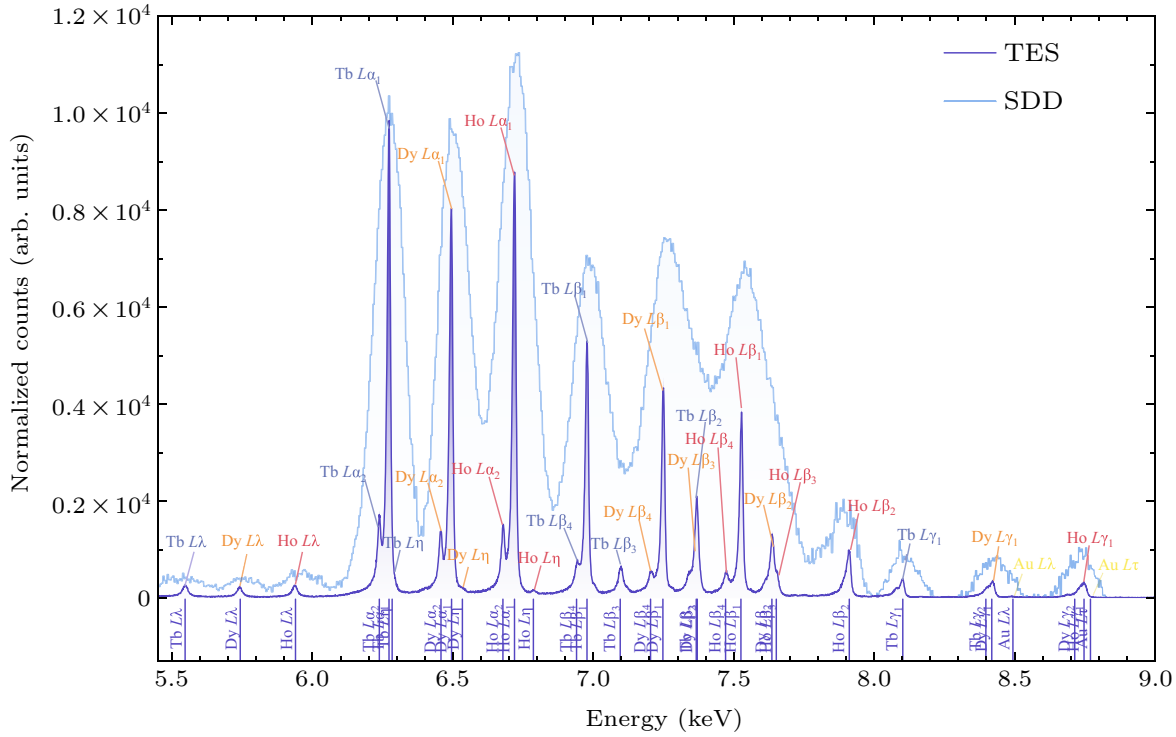


Fig. 7. The calibrated *L*-edge emission spectrum of the mixed sample of all REOs. The spectrum obtained by our spectrometer of TES (purple) is compared with the spectrum obtained under similar conditions by SDD detector (blue). The TES spectrum is the average result of all valid channels, with the standard deviation plotted as its margin. Vertical lines with elemental peak labels at the bottom of the figure indicate the energies of the *L*-edge emission lines of REEs. Data are collected from NIST database.[26,27]

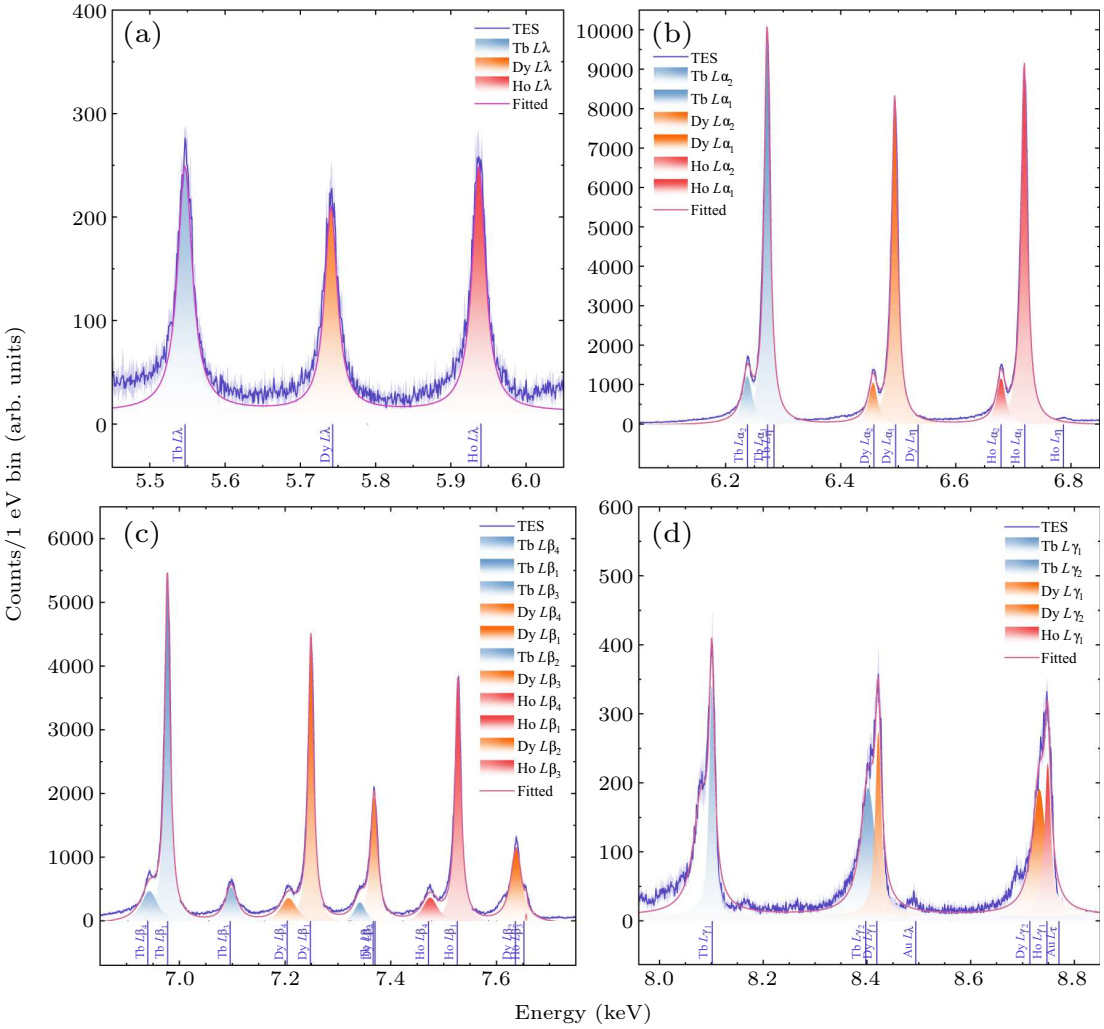


Fig. 8. The respective peak fitting results of each region of the average spectrum of all REOs. Original data are purple lines with the standard deviation margin, and fitted lines of different regions are plotted as magenta lines. The Lorentz function is chosen as the fitting function, while the energy resolution is under certain restrictions. (a) The fitting result of the measured spectrum in the energy range of $L\lambda$ regions. (b) The fitting result of the measured spectrum in the energy range of $L\alpha$ and $L\eta$ regions, as $L\alpha_1$ and $L\alpha_2$ peaks are separated accordingly. (c) The fitting result of the measured spectrum in the energy range of $L\beta$ regions, as each of the peaks of the overlapping parts is also separated accordingly. (d) The fitting result of the measured spectrum in the energy range of $L\gamma$ regions, with some of the L-edge peaks contributed by Au anode target ignored.

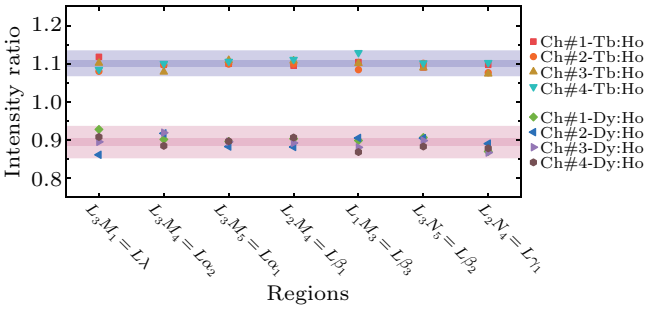


Fig. 9. The intensity comparison result for regions of Tb:Ho and Dy:Ho across part of the TES channels. The intensity ratio can be calculated from the proportional relationship between the fitted areas of different regions. The total detection efficiency is taken into consideration as well. It shows small statistical fluctuation between different channels, while the fluctuation seems to be less obvious in larger areas of the region in Fig. 8, i.e., a more stable proportional coefficient can be obtained.

4. Conclusion

We have described the XRF spectroscopy measurement of REEs, by the newly developed spectrometer consisting of an array of 16-pixel (4×4) superconducting TESs with an energy resolution of 5.2 eV@5.9 keV. Further, we have developed an analytical methodology for material with REEs to figure out the element composition of each REE and its proportion according to the energy spectrum with higher accuracy. In this paper, we have explained the structures, principles and components of the spectrometer, and have elaborated the detailed process of our experiment. The XRF spectrum of evenly mixed samples of oxide components of terbium, dysprosium and holmium are obtained and well calculated out, with energy peaks fitted respectively and analyzed afterwards. According to the result of chemical component analysis, an XRF coefficient database of fitted spectrum peaks of REEs can be established. These measurements and analyses pose an update for the conventional XRF methodology, which could be extremely valuable for digging out the unrevealed energy lines and processes. In the future, through the measured data of XRF spectroscopic analysis of REOs, we can obtain informa-

tion of various REEs. This methodology can be implemented into practical analyzing experiments for rare earth functional material, which contains trace level REEs and is sensitive to the slight changes in the doping proportion. We believe it can provide some powerful assistance in some cases of as yet undefined compositional analyses. Additionally, it has the potential to provide references for further applications, such as characterizing rare earth materials, analyzing their compositions, and aiding in resource development. Furthermore, the measurement is conducted using an x-ray tube with extremely low power, which implies that the TES-based spectrometer exhibits a high energy resolution and sensitivity, allowing some experiments that conventionally require synchrotron radiation sources to be conducted in small-scale laboratories, thus reducing the barriers for measurement.

Acknowledgments

Project supported by the National Major Scientific Research Instrument Development Project (Grant No. 11927805), the National Key Research and Development Program of China (Grant No. 2022YFF0608303), the NSFC Young Scientists Fund (Grant No. 12005134), the Shanghai-XFEL Beamline Project (SBP) (Grant No. 3101150550588592016 1A2101001), and the Shanghai Municipal Science and Technology Major Project (Grant No. 2017SHZDZX02).

References

[1] Hoshino M, Sanematsu K and Watanabe Y 2016 *Handb. Phys. Chem. Rare Earths* **49** 129
[2] Aide M T and Aide C 2012 *ISRN Soil Sci.* **2012** e783876
[3] Xie J, Zhang M, Wang Y, Guo R, Shi Y, Pan X, Liu X, Chen K, Tang M, Wu F and Zhang Z 2022 *J. Rare Earths* **40** 1706
[4] Matjaž K 2012 *X-Ray Spectroscopy* (Rijeka: IntechOpen) pp. 81–98
[5] Röhler J 1987 *Handb. Phys. Chem. Rare Earths* **10** 453
[6] Uhlig J, Doriese W B, Fowler J W, *et al.* 2015 *J. Synchrotron Radiat.* **22** 766
[7] Henke B L, Gullikson E M and Davis J C 1993 *At. Data Nucl. Data Tables* **54** 181
[8] Newbury D E and Ritchie N W M 2015 *J. Mater. Sci.* **50** 493
[9] Silva C D, Santana G P and Paz S P A 2020 *Talanta* **206** 120254
[10] Carlos A C, Jose A T A and Maria A C J 2012 *X-Ray Spectroscopy* (Rijeka: IntechOpen) pp. 119–136
[11] Yamada K, Kawakami N, Moronaga T, Hayashi K, Ichihara C and Hara T 2020 *Appl. Phys. Express* **13** 082008
[12] Rafał S and Beata Z 2012 *X-Ray Spectroscopy* (Rijeka: IntechOpen) pp. 137–162
[13] Kirsanov D, Panchuk V, Goydenko A, Khaydukova M, Semenov V and Legin A 2015 *Spectrochim. Acta Part B: At. Spectrosc.* **113** 126
[14] Smoliński A, Stempin M and Howaniec N 2016 *Spectrochim. Acta Part B: At. Spectrosc.* **116** 63
[15] Wu W, Xu T, Hao Q, Wang Q, Zhang S and Zhao C 2010 *J. Rare Earths* **28** 30
[16] Zhang S, Xia J, Wu W, Song Y, Wu B and Liu Z 2022 *Eighth Symposium on Novel Photoelectronic Detection Technology and Applications*, November 10–12, 2021, Kunming, China, p. 381
[17] Xia J, Zhang S, Yang J, Song Y and Liu Z 2022 *J. Low Temp. Phys.* **209** 1017
[18] Xia J, Zhang S, Wu B and Liu Z 2022 *Eighth Symposium on Novel Photoelectronic Detection Technology and Applications*, November 10–12, 2021, Kunming, China, p. 2051
[19] Zhang S, Xia J and Wu B 2022 *Eighth Symposium on Novel Photoelectronic Detection Technology and Applications*, November 10–12, 2021, Kunming, China, p. 369
[20] Zhang S, Xia J, Sun T, Wu W, Wu B, Wang Y, Cantor R, Han K, Zhou X, Liu H, Fan F, Guo S, Liang J, Li D, Song Y, Ju X, Fu Q and Liu Z 2022 *Nucl. Sci. Tech.* **33** 84
[21] Zhang S, Cui W, Jin H, Chen L, Wang J, Wu W, Wu B, Xia J, Song Y, Yang J, Weng T and Liu Z 2021 *Acta Phys. Sin.* **70** 180702 (in Chinese)
[22] Wu W, Lin Z, Ni Z, Li P, Liang T, Zhang G, Wang Y, Ying L, Peng W, Zhang W, Shi S, You L and Wang Z 2022 *Chin. Phys. B* **31** 028504
[23] Zhang Q, Wang T, Liu J, Dong W, He G, Li T, Zhou X and Chen W 2014 *Chin. Phys. B* **23** 118502
[24] Titus C J, Baker M L, Lee S J, *et al.* 2017 *J. Chem. Phys.* **147** 214201
[25] Friedrich S 2006 *J. Synchrotron Radiat.* **13** 159
[26] Deslattes R D, Kessler E G, Indelicato P, de Billy L, Lindroth E, Anton J, Coursey J S, Schwab D J, Chang C, Sukumar R, Olsen K and Dragoset R A *NIST X-Ray Transition Energies Database*
[27] Deslattes R D, Kessler E G, Indelicato P, de Billy L, Lindroth E and Anton J 2003 *Rev. Mod. Phys.* **75** 35
[28] McCammon D 2005 *Cryogenic Particle Detection* (Heidelberg: Springer) pp. 1–34
[29] Irwin K and Hilton G 2005 *Cryogenic Particle Detection* (Heidelberg: Springer) pp. 63–150
[30] Gottardi L and Nagayashi K 2021 *Appl. Sci.* **11** 3793
[31] Yu Q, Zhang Y, Zhao C, He K, Huang R, He Y, Wu X, Liu J and Chen W 2021 *Chin. Phys. B* **30** 077402
[32] Moseley S H, Mather J C and McCammon D 1984 *J. Appl. Phys.* **56** 1257
[33] Henke B L, Gullikson E M and Davis J C *X-Ray Filter Transmission*
[34] Doriese W B, Abbamonte P, Alpert B K, *et al.* 2017 *Rev. Sci. Instrum.* **88** 053108
[35] Fowler J W, O'Neil G C, Alpert B K, Bennett D A, Denison E V, Doriese W B, Hilton G C, Hudson L T, Joe Y I, Morgan K M, Schmidt D R, Swetz D S, Szabo C I and Ullom J N 2021 *Metrologia* **58** 015016
[36] Lee S J, Titus C J, Alonso M R, *et al.* 2019 *Rev. Sci. Instrum.* **90** 113101
[37] Illig A J, Chantler C T and Payne A T 2013 *J. Phys. B: At. Mol. Opt. Phys.* **46** 235001